

1 **A novel deep learning-based point-of-care diagnostic method for detecting *Plasmodium***  
2 ***falciparum* with fluorescence digital microscopy**

3 O. Holmström<sup>1\*</sup>, S. Stenman<sup>1</sup>, A. Suutala<sup>1</sup>, H. Moilanen<sup>2</sup>, H. Kücükkel<sup>1</sup>, B. Ngasala<sup>3,4</sup>, A. Mårtensson<sup>3</sup>,  
4 L. Mhamilawa<sup>3,4</sup>, B. Aydin-Schmidt<sup>5</sup>, M. Lundin<sup>1</sup>, V. Diwan<sup>6</sup>, N. Linder<sup>1,3\*</sup>, J. Lundin<sup>1,6\*</sup>

5

6 <sup>1</sup>Institute for Molecular Medicine Finland (FIMM), P.O. Box 20, FI-00014, University  
7 of Helsinki, Helsinki, Finland

8 <sup>2</sup>Center of Microscopy and Nanotechnology, University of Oulu, Finland

9 <sup>3</sup>Department of Women's and Children's Health, International Maternal and Child Health (IMCH),  
10 Uppsala University, Sweden

11 <sup>4</sup>Department of Medical Entomology and Parasitology, School of Public Health, Muhimbili  
12 University of Health and Allied Sciences, Dar es Salaam, Tanzania

13 <sup>5</sup>Department of Microbiology, Tumor and Cell Biology, Karolinska Institutet, Stockholm, Sweden

14 <sup>6</sup>Department of Global Public Health, Karolinska Institutet, Stockholm, Sweden

15

16

17 Corresponding author: Johan Lundin, Institute for Molecular Medicine Finland

18 (FIMM), P.O. Box 20, FI-00014, University of Helsinki, Finland, E-mail: [johan.lundin@helsinki.fi](mailto:johan.lundin@helsinki.fi)

19

20 **Short running title:** Point-of-care fluorescence microscopy and deep learning for malaria diagnostics

21 **Key words:** Point-of-care testing, Malaria, Computer-aided Diagnosis, Deep learning, Fluorescence  
22 microscopy.

23

24 **Word count of abstract: 295**

25

26 **Abstract**

27 **Background** Malaria remains a major global health problem with a need for improved field-usable

28 diagnostic tests. We have developed a portable, low-cost digital microscope scanner, capable of both

29 brightfield and fluorescence imaging. Here, we used the instrument to digitize blood smears, and  
30 applied deep learning (DL) algorithms to detect *Plasmodium falciparum* parasites. **Methods** Thin  
31 blood smears ( $n = 125$ ) were collected from patients with microscopy-confirmed *P. falciparum*  
32 infections in rural Tanzania, prior to and after initiation of artemisinin-based combination therapy.  
33 The samples were stained using the 4',6-diamidino-2-phenylindole fluorogen and digitized using the  
34 prototype microscope scanner. Two DL algorithms were trained to detect malaria parasites in the  
35 samples, and results compared to the visual assessment of both the digitized samples, and the Giemsa-  
36 stained thick smears. **Results** Detection of *P. falciparum* parasites in the digitized thin blood smears  
37 was possible both by visual assessment and by DL-based analysis with a strong correlation in results  
38 ( $r = 0.99$ ,  $p < 0.01$ ). A moderately strong correlation was observed between the DL-based thin smear  
39 analysis and the visual thick smear-analysis ( $r = 0.74$ ,  $p < 0.01$ ). Low levels of parasites were detected  
40 by DL-based analysis on day three following treatment initiation, but a small number of fluorescent  
41 signals were detected also in microscopy-negative samples. **Conclusion** Quantification of *P.*  
42 *falciparum* parasites in DAPI-stained thin smears is feasible using DL-supported, point-of-care digital  
43 microscopy, with a high correlation to visual assessment of samples. Fluorescent signals from  
44 artefacts in samples with low infection levels represented the main challenge for the digital analysis,  
45 thus highlighting the importance of minimizing sample contaminations. The proposed method could  
46 support malaria diagnostics and monitoring of treatment response through automated quantification of  
47 parasitaemia and is likely to be applicable also for diagnostics of other *Plasmodium* species and other  
48 infectious diseases.

49

## 50 **1 Introduction**

51 Malaria remains a global health burden with over 200 million new yearly cases (1). Although the  
52 disease incidence has decreased by approximately 10% during the last decade, data indicates that  
53 progress has stalled during recent years (1). As most malaria cases occur in rural areas (1), the disease  
54 burden is caused partly by difficulties in diagnosing the disease. Currently, multiple techniques exist  
55 for malaria diagnostics (2). Light microscopy assessment of blood smears to detect *Plasmodium*

56 parasites remains the diagnostic golden standard (3) and allows detection and quantification of the  
57 various *Plasmodium* species while also being more sensitive than rapid diagnostic tests (RDTs) (4).  
58 Disadvantages with microscopy-based testing include a high level of labour intensiveness,  
59 subjectivity (5, 6), dependence on the microscopist's skill and experience (7), requirements in terms  
60 of sample preparation and varying sensitivity for lower-level and mixed infections (4). In addition to  
61 microscopy, easy-to-use RDTs based on lateral flow immunochromatography to detect *Plasmodium*-  
62 specific antigens are being used to an increasing extent (8). These RDTs enable rapid diagnostics at  
63 the point-of-care (POC), but have limited accuracy for non-*falciparum* (2) and low-level infections,  
64 do not allow for quantification of parasites when monitoring treatment response, and remain positive  
65 after treatment initiation, which means that results should ideally be validated by other methods (4).  
66 Detection of *Plasmodium* spp. nucleic acid with nucleic acid amplification tests (NAATs) has  
67 superior analytical sensitivity compared to other methods, especially for mixed infections (9), and  
68 allows quantification of parasitaemia (by real-time quantitative polymerase chain reaction; qPCR) but  
69 is more technically demanding, expensive and therefore not widely available (4), although certain  
70 NAAT-methods, such as loop-mediated isothermal amplification (LAMP) show promise as a field-  
71 usable techniques (10). Consequently, the World Health Organization (WHO) currently recommends  
72 microscopy-based methods to confirm diagnosis in suspected cases of malaria (3). Various staining  
73 methods have been proposed for microscopy identification of malaria parasites in blood smears, with  
74 Giemsa staining being the standard method (5). As visual analysis of blood smears is time-consuming  
75 and subjective, fluorescent staining methods have been proposed to facilitate the sample analysis  
76 process (11). Cell-permeable fluorescent stains can be used to visualize the intracellular *Plasmodium*  
77 parasites more clearly and at lower magnification (12) to reduce the need for high-power microscopy  
78 equipment. Fluorescent stainings can also be combined with brightfield staining protocols (11). As  
79 access to microscopy diagnostics is severely limited in many areas, the potential to utilize optical  
80 components from widely-available consumer electronic products (such as smartphone cameras) to  
81 create digital microscopes has been recognized (13 - 15). By utilizing miniaturized, low-cost  
82 optomechanical components, several devices for POC digitization of microscopy slides have been  
83 developed. Compared to larger-sized, laboratory-grade slide scanners, these types of devices can be

84 manufactured significantly cheaper (16) and have other potential advantages, such as a smaller  
85 physical size for increased portability, which make them potentially more suitable for POC usage.  
86 Although these components are significantly less expensive than those used in high-end alternatives,  
87 the imaging performance achievable is sufficient to e.g. visualize pathogens in common infectious  
88 diseases (17) and for analysis of histological samples (18). Digitization of samples at the POC  
89 combined with the mobile connectivity of the instruments also mean that samples can be uploaded to  
90 a cloud server for remote access and analysis using digital methods (19). Multiple approaches have  
91 been studied for automated, computer-assisted diagnosis of malaria using both traditional computer  
92 vision methods and more recently machine learning algorithms based on deep convolutional neural  
93 networks (20-22). Several efforts have been made to digitize blood smears for malaria diagnostics  
94 with POC slide scanners, but a significant challenge with conventionally-stained samples is the need  
95 for higher magnifications than what is typically supported by these platforms (21).

96 In this proof-of-concept study we describe how thin blood smears acquired in field-settings in  
97 Tanzania, stained with the 4',6-diamidino-2-phenylindole (DAPI) fluorophore and scanned using a  
98 low-cost POC digital microscope scanner prototype enables visualization of *P. falciparum* parasites.  
99 *P. falciparum* is both the most prevalent malaria parasite in Africa, and the cause of the vast majority  
100 of malaria-related deaths (1). By digitizing both brightfield and fluorescent image channels from  
101 blood smears, and combining them into hybrid images, intracellular malaria parasites can be  
102 visualized in the digital samples. Furthermore, we train and apply two separate deep-learning  
103 algorithms to automatically detect and quantify *P. falciparum* trophozoites in the digital samples.  
104 Results are compared to the visual analysis of the digital samples and to expert microscopy of  
105 Giemsa-stained thick smears, using samples collected on the day of initiation of artemisinin-based  
106 combination therapy (ACT) and three days after treatment initiation.

## 107 **2 Materials and Methods**

### 108 **2.1 Acquisition and preparation of samples**

109 We acquired 125 thin blood films for this study, which were collected as part of the trial by  
110 Mhamilawa et al. (23). The overall study workflow and sample analysis process is illustrated as a  
111 STARD diagram in the supplementary material (S Fig 6). The samples were collected in a region with  
112 moderate levels of malaria transmission where *P. falciparum* is the predominant species (Bagamoyo  
113 District, Tanzania) during a time-period between July 2017 and March 2018. Samples were collected  
114 from volunteering patients who fulfilled the inclusion criteria (age between 1 and 65 years, history of  
115 fever in the last 24 hours or axillary temperature  $\geq 37.5$  °C, microscopy-confirmed uncomplicated *P.*  
116 *falciparum* monoinfection and written informed consent obtained). Microscopy confirmation of  
117 malaria positivity was performed on separate Giemsa-stained thick blood smears by certified  
118 professional microscopists. The number of asexual parasites and gametocytes was determined by  
119 counting the number of visible parasites per 200 white blood cells (WBCs) using a hand tally counter.  
120 The parasite density, measured as the number of asexual parasites per microliter ( $\mu$ l) of blood, was  
121 estimated by dividing the number of detected asexual parasites per by the number of WBCs counted  
122 (200) and multiplying the value by the assumed WBC count  $\mu$ l of blood (8,000 WBC/ $\mu$ l). A blood  
123 smear was considered negative after examining 100 high-power fields or counting 500 WBC with no  
124 parasites seen. Each slide was read by two independent and experienced microscopists, and upon  
125 disagreement on presence of parasites or if density differed by more than 25%, the slides were  
126 subjected to a third independent and decisive reader (blinded to the results from the previous readers).  
127 The mean parasitemia of the two most concordant readings were used as final parasite densities. In  
128 total, 125 unstained thin blood films from 100 separate patients were obtained for this study. 100 of  
129 these samples were collected before initiation of artemisinin-based combination therapy (ACT) (Day  
130 0), and 25 samples were follow-up thin blood smears collected three days after initiation of ACT (Day  
131 3). The Day 3 samples were also analysed by light microscopy examination, according to the  
132 procedure described above. Samples were fixated with methanol (water < 3 %) by incubating for

133 approximately 20 minutes at room temperature, and stored in slide boxes following this. For the  
134 staining of the samples, the slides were initially rinsed with deionized water, after which staining of  
135 the samples was performed using a mounting media solution containing 4',6-Diamidino-2-  
136 phenylindole (DAPI) fluorescent stain (Fluoroshield with DAPI, Sigma-Aldrich Finland Oy, Espoo,  
137 Finland). DAPI is a counterstain for DNA and RNA which penetrates cellular membranes to stain the  
138 DNA (and RNA) of the *Plasmodium* parasites inside intact erythrocytes. The DAPI staining solution  
139 was applied to the sample and distributed over the surface of the glass slide. Following this, the  
140 sample was let to stand at room temperature for five minutes, after which a cover slip was carefully  
141 applied to the sample to avoid air bubbles. After staining, the quality of the sample was examined  
142 visually with a fluorescence microscope to confirm that the staining quality was adequate for analysis  
143 (i.e. visible fluorescent WBCs to confirm successful staining and low amounts of debris).

## 144 **2.2 Digitization of slides**

145 For the digitization of the samples we used a prototype of a portable, digital microscope scanner,  
146 developed and patented by the University of Helsinki (Helsinki, Finland) for POC scanning of  
147 biological samples (Fig 1). The device supports brightfield and fluorescent imaging of glass slides and  
148 scanning of sample areas measuring multiple fields of view (FOVs), by capturing and stitching  
149 together multiple FOVs in a similar way as conventional whole-slide microscopy scanners. The  
150 device is constructed using inexpensive plastic optomechanical components from consumer electronic  
151 products. Total material costs for the components are comparable to the price of a mid-range  
152 smartphone (approximately 500 - 1000 EUR), and significantly lower than the prices of conventional  
153 slide scanners with device costs typically between 50.000 to 300.000 USD (16).

154

155 **Figure 1.** (a) The prototype digital slide scanner (1) with slide adjustment motor unit (2) and laptop  
156 computer used to control device (3). (b) USAF standardized resolution test chart, digitized with the  
157 microscope prototype, showing the smallest set of resolvable bars (corresponding to a spatial  
158 resolution of 0.9  $\mu\text{m}$ ).

159

160 Digital images are captured using a camera module typically used in smartphone camera systems  
161 (See3CAM\_130, e-con Systems Inc., St Louis, USA), featuring a 13-megapixel (maximum resolution  
162 4208 x 3120 pixels) complementary metal oxide semiconductor (CMOS) sensor with a plastic 1/3.2”  
163 lens. A white light-emitting diode (LED) is used as the light source for brightfield imaging and an  
164 ultraviolet LED combined with a retractable band pass filter for fluorescent imaging (peak wavelength  
165 365 nm). If the FOV is digitized using both the brightfield and fluorescence modes of the microscope,  
166 the resulting image can be rendered into a single merged image. (Fig 2).

167

168 **Figure 2.** Microscopic field of view (FOV), showing the corresponding (a) brightfield, (b)  
169 fluorescence and (c) merged thin blood smear digital images. Red bounding boxes showing enlarged  
170 areas with (1) infected red blood cells (RBCs), (2) normal RBCs, (3) leukocytes and (4) fluorescent  
171 debris.

172

173 With the current image sensor and lens, the pixel size was 0.22  $\mu\text{m}$  and the spatial resolution 0.9  $\mu\text{m}$ ,  
174 as measured using a standardized USAF resolution test chart and white-light LED illumination (Fig  
175 1). One sensor FOV measures 0.22  $\text{mm}^2$  (4208 x 3120 pixels), which is approximately five times  
176 larger than the FOV of a typical 100x objective (0.22 $\text{mm}^2$  compared to 0.04 $\text{mm}^2$ ).

177 The device is connected to and operated from a computer by universal serial bus (USB), which also  
178 provides power for the device. An external motor unit (Fig 2) is used to move the sample holder with  
179 the glass slide to scan the sample. Coarse focus can be adjusted with a manual focus lever and fine  
180 focus with the built-in autofocus routine of the camera module. The device is controlled with a custom  
181 software written in the matrix laboratory (MATLAB, MathWorks Inc, Natick, MA) computing and  
182 programming environment, which features a live view from the camera feed, overview of scanned  
183 areas and controls for adjusting parameters of slide scanning (e.g. area to be captured, focus and  
184 exposure). Digitization of areas measuring more than one FOV utilizes the motor unit for automatic  
185 slide translation while the camera captures multiple images. The individual digitized samples in this

186 study measured 12-20 FOVs per sample, representing a thin smear area (red blood cell [RBC]  
187 monolayer) without significant amounts of artefacts or debris when examined visually) of 2.65-4.41  
188 mm<sup>2</sup>. This corresponds to approximately 80-140 optical microscopy FOVs, using a conventional 100  
189 x magnification (24). Image files were saved locally in the Tagged Image File Format (TIFF) and  
190 converted to a wavelet file format (Enhanced Compressed Wavelet, ECW, ER Mapper, Intergraph,  
191 Atlanta, Georgia) with a compression ratio of 1:9, before uploading to the image management  
192 platform (Aiforia Cloud, Aiforia Technologies Oy, Helsinki, Finland). This amount of compression  
193 has been shown in earlier studies to preserve sufficient detail to not alter results significantly (25).  
194 Remote access to the image server for sample viewing is established using a web browser, secured  
195 with Secure Socket Layer (SSL).

### 196 **2.3 Visual analysis of digital samples and training of deep learning systems**

197 Samples were visually evaluated by two researchers (O.H. and S.S), who independently reviewed the  
198 digital samples on an LCD computer monitor and counted all visible *Plasmodium* parasites in the  
199 images. Parasites were manually annotated on the slide-management platform and the annotations  
200 served as ground truth for the digital image analysis. Sample parasitaemia was calculated as the  
201 number of detected parasites divided by the number of red blood cells (RBCs) detected by digital  
202 image analysis as described below. Results were recorded in a spreadsheet table (Microsoft Excel,  
203 Microsoft, Redmond WA).

204 For the digital analysis of the samples we trained two separate image analysis algorithms, based on  
205 deep learning (DL) with deep convolutional neural networks (CNNs). We utilized manually annotated  
206 image regions (n = 1,176) from a subset of thin blood smears (n = 25) to train the algorithms to detect  
207 visible malaria trophozoites and RBCs.

208 For the first deep-learning system (DLS 1), the digitized samples were uploaded to a  
209 commercially available, cloud-based machine-learning platform (Aiforia Cloud and Create, Aiforia  
210 Technologies Oy, Helsinki, Finland). Using this platform, a supervised deep-learning system (DLS)  
211 was trained to detect intracellular trophozoites in the digital images. For this method, the



212 corresponding brightfield and fluorescence image channels were merged into hybrid images (Fig 3).  
213 The training data was visually reviewed by a researcher (S.S.), and visible trophozoites and RBCs  
214 were annotated to constitute the training data. This system consists of two sequential CNN algorithms.  
215 The first algorithm detects all RBCs (i.e. infected and non-infected). The corresponding results are  
216 then forwarded to a second layer, containing two separate algorithms; one that detects infected RBCs  
217 (RBCs with visible fluorescent intracellular trophozoites; i.e. parasite candidates) and one that detects  
218 non-infected RBCs (RBCs without visible parasite candidates). The sample parasitaemia is calculated  
219 as the number of detected parasites divided by the total number of detected RBCs (Fig 2). To increase  
220 the generalisability of the model, digital image augmentations by perturbation of the training data  
221 were utilized. In the first CNN layer, augmentations used were rotation (0-360°), variation of scale  
222 ( $\pm 10\%$ ), shear distortion ( $\pm 10\%$ ), aspect ratio ( $\pm 10\%$ ), contrast ( $\pm 10\%$ ), white balance ( $\pm 10\%$ ) and  
223 luminance ( $\pm 10\%$ ). In the second layer, the training material was augmented by rotation (0-360°),  
224 variation of scale ( $\pm 5\%$ ), shear distortion ( $\pm 5\%$ ), aspect ratio ( $\pm 5\%$ ), contrast ( $\pm 5\%$ ), white balance  
225 ( $\pm 5\%$ ) and luminance ( $\pm 5\%$ ). Training of the model was performed with 7,584 completed iterations  
226 (training epochs) of training and a predetermined feature size for object classification of 7  $\mu\text{m}$  (RBCs)  
227 and 3  $\mu\text{m}$  (parasites), using an image analysis window size (FOV) of 15  $\mu\text{m}$ .

228

229

230 **Figure 3.** Workflow for training of the first deep-learning system (DLS 1) and subsequent analysis of  
231 samples using the trained model. (a): Training of the DLS was performed on merged images  
232 (brightfield and fluorescent images combined) where regions with visible red blood cells (RBCs) and  
233 trophozoites (parasites) were manually annotated and used to train the DLS to detect RBCs and  
234 classify them as infected vs. non-infected. (b): Analysis of samples in the validation series was  
235 performed on merged images in two steps: 1) Segmentation of all visible RBCs and 2) quantification  
236 of infected and non-infected RBCs to determine overall level of parasitaemia.

237 The second deep-learning system (DLS 2) analysis method also utilizes deep learning with  
238 CNNs, and analyses the brightfield and fluorescence images from the sample separately. The

239 workflow of this system is described in Figure 3. First, the RBCs in the brightfield-only image are  
240 identified using circle Hough Transform (CHT) to allow the selection of individual, well-preserved  
241 RBCs, while avoiding overlapping, clumped or otherwise deformed cells. Subsequently, a normalized  
242 cross correlation and peak finding algorithm (26) identifies the locations matching with a parasite  
243 template in the corresponding fluorescence-only image where the correlation peaks represent the  
244 centroids of the parasite candidates. Selected RBCs are then used to create a quantitation mask, and  
245 by combining the data from both images the parasite candidates are then addressed to the selected  
246 individual RBCs in the merged image. Notably, only the detected fluorescence signals emitted from  
247 locations inside the RBCs are included (with a small margin to cover the applique parasite forms and  
248 possible optical misalignment of the image channels). This also enables the detection of multiple  
249 objects within a single RBC; such as multiple visible parasites. A threshold was determined for the  
250 cross-correlation coefficient and Structural Similarity Index (SSIM) (27) value of the candidates to  
251 reduce computation cost by not including the least likely parasite objects, i.e. weak signals emitting  
252 from the background fluorescence. The SSIM Index assesses the visual impact of luminance, contrast  
253 and structure characteristics of an image.

254

255 **Figure 4.** Workflow of training and analysis with the second deep-learning system (DLS 2) using the  
256 GoogLeNet model. Panels showing brightfield images with segmented red blood cells (RBCs), the  
257 corresponding fluorescence image with detected parasite candidates, classification of parasites and  
258 exported analysis results.

259 For the classification part, transfer learning (28) was utilized using a pre-trained GoogLeNet  
260 network (29) The model is a binary-classification CNN which was trained using manually selected  
261 image-regions from the training series of samples, representing visible parasites and non-parasite  
262 fluorescent objects (i.e. debris and other artefacts). The training data was visually reviewed by a  
263 researcher (AS), and visible trophozoites (n = 5059) and other fluorescence signals (n = 856) were  
264 annotated from the training samples to constitute the training data for the two classes. As the

265 parasitaemia level was relatively high in a large part of the training samples, the number of true  
266 parasites was significantly higher than the number representing other fluorescence signals. To reduce  
267 training imbalance and to ensure that high-parasitaemia samples would not dominate the training  
268 while preserving a sufficiently diverse distribution of parasites, the number of parasites selected from  
269 each training sample was limited based on the SSIM value of the candidate objects. Specifically, in  
270 each training sample, only the candidates with a unique SSIM value were included in the training.  
271 Rotation (0 - 360°) and variation of scale ( $\pm 5\%$ ) were utilized to augment image data, to prevent  
272 overfitting. Training of the model was performed in 30 training epochs with a batch size of 32 using a  
273 stochastic gradient descent solver with a momentum of 0.9 and initial learning rate of 0.0003. During  
274 the analysis phase the RBC was marked infected if at least one addressed parasite candidate was  
275 classified as a trophozoite with a classification score of at least 95/100. The overall parasitaemia was  
276 determined by the ratio of infected RBCs to the total number of RBCs (S Fig 1). DLS 2 is run locally  
277 and therefore suitable for potential integration directly into e.g. the imaging system for rapid analysis.

## 278 **2.5 Statistical analysis**

279 Statistical analysis of results was performed using a general-purpose statistical software package  
280 (Stata 15.1 for Mac, Stata Corp., College Station, TX, USA). We calculated a Pearson's product-  
281 moment correlation to determine the relationship between parasitaemia determined by visual  
282 examination and analysis with the deep learning models in the digital samples. We utilized a two-  
283 sided paired Wilcoxon Signed-Rank test to assess the difference in detected levels of parasitaemia  
284 between the Day 0 and Day 3 samples. Power analysis for these calculations were conducted using the  
285 G\*Power software v3.1.7 (Universität Kiel, Kiel, Germany) to determine a sufficient sample size,  
286 using an alpha of 0.05, a power of 0.95 and an effect size of 1.17 (as calculated based on the  
287 difference between visually-determined levels of parasitaemia in slide pairs from the training data),  
288 which yielded a minimum required number of samples of 34 (17 slide pairs) (30).

289

## 290 **2.6 Ethical statement**

291 Ethical clearance for the study was issued by the National Institute for Medical Research and  
292 Muhimbili University of Health and Allied Sciences, Tanzania (Identifier: NCT03241901).

## 293 **3 Results**

### 294 **3.1 Quantification of parasites in digital samples**

295 Prior to analysis of the main samples used in the study, we tested the image capture and algorithms on  
296 a series of test blood thin smears, prepared in laboratory conditions from blood cultures with known  
297 levels of *P. falciparum* infection (n = 7; approximately 0%, 0.2%, 0.5%, 1% and 2%, respectively).  
298 Here, we confirmed that fluorescent parasites and parasitized red blood cells (RBCs) could be  
299 visualized at the spatial resolution provided by the instrument. Overall, we observed a high level of  
300 similarity and almost perfect correlation between the DLS-based sample analysis and the known  
301 infection levels of the samples ( $r(7) = 0.99$ ,  $p < 0.001$ ) (S Fig 4).

302 For the samples used in the study, after exclusion of samples used for the training of the deep-  
303 learning systems, 97 samples remained in the validation series, of which 77 samples were thin blood  
304 smears collected at baseline, prior to initiation of treatment with ACT (Day 0), and 20 samples were  
305 follow-up thin blood smears collected on day 3 after treatment initiation (Day 3). All samples  
306 collected on day 0 were confirmed as malaria-positive by light-microscopy assessment of thick  
307 smears from the same patients, with a mean parasitaemia of 58,711 parasites/ $\mu$ L (95%CI 44,055 -  
308 73,368 parasites/ $\mu$ L) and correspondingly a mean estimated parasitaemia of 1.17 % (95% CI 0.88 -  
309 1.47). The follow-up samples on day 3 after treatment initiation were all confirmed microscopy  
310 negative for malaria (no visible parasites in the Giemsa thick smear). The visual analysis of all  
311 fluorescently-stained digitized day 0 thin smears revealed visible parasites, with an overall mean rate  
312 of infected RBCs of 1.79 % (CI95% 1.31 - 2.26%). The visual analysis of the Day 3 digital samples  
313 detected a significantly lower rate of infected RBCs (0.014%, 95%CI 0.009 - 0.009 - 0.020%,  $z = -$   
314 3.92,  $p < 0.001$ ). The DLS analysis of the digitized thin smears returned similar levels of detected

315 infected RBCs as the visual analysis of the digital samples in all analysed microscopy-positive

316 samples (mean 1.70% [95%CI 1.27 - 2.15%] and 1.76% [95% CI 1.32 - 2.20%]) (Table 1).

317

318 **Table 1.** Results from analysis of blood samples by light microscopy of Giemsa-stained thick smears,

319 visual analysis of digitized DAPI-stained samples and DLS-based analysis of the digitized DAPI-

320 stained samples. Parasitaemia estimated as the rate of infected red blood cells (RBCs), multiplied by

321 the assumed number of RBCs per  $\mu$ l of blood (5,000,000).

322

Diagnostic comparison	Visual analysis of digitized thin smears	DLS1 analysis of digitized thin smears	DLS2 analysis of digitized thin smears	Microscopy thick-smear analysis (Giemsa)
<b>Day 0</b>				
Number of samples	77	77	77	77
Mean number of parasites detected per analysed area (n, 95% CI)	398 (297 - 498)	396 (295 - 496)	348 (261 - 436)	n/a*
Percentage of infected RBCs (% , 95% CI)	1.79 (1.31 - 2.26)	1.70 (1.27 - 2.15)	1.76 (1.32 - 2.20)	1.17 (0.88 - 1.47)
Mean estimated parasitemia (throphozoites/ $\mu$ L , 95% CI)	89,500 (65,500 - 113,000) **	85,000 (63,500 - 107,500) **	88,000 (66,000 - 110,000) **	58,711 (44,054 - 73,368)
<b>Day 3</b>				
Number of samples	20	20	20	20
Mean number of parasites detected per analysed area (n, 95% CI)	3 (2 - 4)	11 (4 - 17)	9 (2 - 16)	0
Percentage of infected RBCs (% , 95% CI)	0.01 (0.01 - 0.02)	0.05 (0.02 - 0.08)	0.05 (0.01-0.09)	0
Mean estimated parasitemia	500 (500 - 1,000) **	2,500 (1,000 - 4,000) **	2,500 (500 - 4,500) **	0

(trophozoites/ $\mu$ L, 95% CI)				
------------------------------------	--	--	--	--

323 \*Not available from thick smear analysis.

324 \*\*Calculated based on the commonly-used approximation of 5,000,000 RBCs per  $\mu$ L.

325

326 The results from the DLS analysis of the Day 3 digitized thin smears also yielded similar values as the  
327 visual sample analysis (mean 0.05% [95%CI 0.017 - 0.083] and 0.05% [95%CI 0.009 - 0.094]). When  
328 assessing correlation between the DLS analysis and the visual analysis of the digital samples, an  
329 almost perfect correlation in detected rate of trophozoites was observed, as calculated with the  
330 Pearson's product-moment correlation coefficient, for the microscopy-positive samples ( $r(77) =$   
331  $0.9996$  and  $0.9986$ ,  $p < 0.01$ ), by analysis with DLS 1 and DLS 2. Compared to the estimated rate of  
332 infected RBCs in the Giemsa thick-smear analysis, the correlation for the DLS 1 and DLS 2 results  
333 were strong ( $r(77) = 0.740$ ,  $p < 0.01$  and  $r(77) = 0.743$ ,  $p < 0.01$ , respectively) (Figure 5).

334 med

335

336 **Figure 5.** Box plots illustrating the detected levels of *P. falciparum* parasitemia (percentage of  
337 infected red blood cells; RBCs) in malaria-positive blood smears collected prior to initiation of  
338 treatment (Day 0) by the deep learning systems (DLS) and by visual analysis of the digital, DAPI-  
339 stained slides and by conventional light microscopy of Giemsa-stained thick smears.

340

341 For the detected rate of infected RBCs in the microscopy-negative samples, a modest correlation was  
342 observed for the DLS-based analysis of samples, compared to the visual sample analysis ( $r(20) = 0.61$   
343 and  $0.42$ ,  $p < 0.01$ ) (Figure 6).

344

345 **Figure 6.** Correlation between levels of *P. falciparum* parasitemia, as detected with the deep learning  
346 systems (DLSs), and by visual analysis of the digital samples, collected on (a) Day 0 and (b) Day 3).

347

348 To further evaluate the DLS-based quantification of *P. falciparum* parasitemia in the Day 0 samples,  
349 we also compared the results from the digital analyses to the level of infection, as determined by  
350 quantitative PCR (qPCR). Here, we also observed a strong correlation between the DLS- and the  
351 qPCR-based assessment of infection level ( $r(27) = 0.90$ ).

352 As qPCR results were only available for a subset of patients (27), these are provided in more detail as  
353 supplementary material (S Fig 3).

354

### 355 **3.2 Monitoring of parasite clearance in thin smears collected at the day of ACT** 356 **treatment initiation and three days later**

357 After exclusion of samples used for training of the image-analysis systems, 40 samples, containing a  
358 total number of 20 pairs of thin smears (Day 0 and Day 3) remained. By expert light microscopy  
359 assessment of the Giemsa-stained thick smears from the same patients, all Day 0 samples ( $n = 20$ )  
360 were classified as positive for *P. falciparum* parasites, and all Day 3 ( $n = 20$ ) samples classified as  
361 negative for visible parasites. Overall, assessed rates of infected RBCs in the Day 3 samples were  
362 significantly lower with all methods studied, than the rates detected in the pre-treatment (Day 0)  
363 samples and the results showed high correlation between the methods studied (Table 1). A Wilcoxon  
364 signed-rank test revealed that the post-treatment (Day 3) parasitaemia of the digitized DAPI-stained  
365 samples was significantly lower than the pre-treatment parasitaemia (Day 0), as determined by visual  
366 analysis (mean: 0.01% [95%CI: 0.01 - 0.02%] vs. 1.76% [CI 95: 1.32 - 2.20],  $z = -3.92$ ,  $p < 0.001$ ),  
367 analysis by DLS 1 (mean: 0.05% [CI 95% 0.02 - 0.08] vs. 1.70% [CI 95% 1.27 - 2.15%],  $z = -3.92$ ,  $p$   
368  $< 0.001$ ) and analysis by DLS 2 (mean: 0.05% [CI 95% 0.01-0.09] vs. 1.76% [CI 95: 1.32 - 2.20],  $z =$   
369  $-3.92$ ,  $p < 0.001$ ) (Figure 7).

370

371 **Figure 7.** Box plots illustrating the detected levels of *P. falciparum* parasitemia (percentage of  
372 infected red blood cells; RBCs) in blood smears collected at baseline, prior to initiation of treatment  
373 (Day 0) and three days following initiation of treatment (Day 3). Results shown as detected by  
374 analysis with the deep learning systems (DLS) and by visual analysis of the digital slides.

375

#### 376 **4 Discussion**

377 In this study we acquired thin blood smears from patients with light microscopy-determined  
378 uncomplicated *P. falciparum* infection, collected at baseline before initiation of artemisinin-based  
379 combination therapy (ACT) and three days following treatment initiation. We stained the samples  
380 using a simplified fluorescent staining protocol and digitized both the fluorescence and brightfield  
381 images into hybrid digital samples, using a small-sized POC digital microscope prototype. The digital  
382 samples were uploaded to a cloud-server and analysed with two deep learning-based systems to detect  
383 and quantify malaria parasites in the samples. Results were compared to visual assessment of the  
384 digitized samples, and to light microscopy examination of Giemsa-stained thick smears. Overall, we  
385 observed strong correlations in the numerical results, i.e. values for detected level of parasitaemia  
386 with the DLS-based system in malaria-positive samples and visual assessment of the digital samples  
387 ( $r = 0.98 - 0.99$ ,  $p < 0.01$ ) and ( $r = 0.42 - 0.61$ ,  $p < 0.01$ ). Compared to the light-microscopy  
388 assessment of Giemsa-stained thick smears, the correlation in detected number of parasites was strong  
389 but lower ( $0.74$ ,  $p < 0.01$ ), likely as the quantification of parasites is not directly comparable when  
390 using different methods of analysis and sample types (thick and thin blood films). Notably, previous  
391 studies have shown that the visual approximation of parasite density in especially thick blood films is  
392 prone to variations, due to factors such as reader technique, quality of slides and the random  
393 distribution of parasites and WBCs (31, 32). Here, both DLSs performed with high similarity to the  
394 manual assessment of the digitized thin smears. When assessing parasite clearance by DLS-based  
395 analysis of digital samples collected on Day 3 after initiation of ACT, significantly lower levels of  
396 parasite candidates were detected in the samples using the digital methods (0.05% vs. 1.73%,  $z = -$   
397 3.92). For quantification of *P. falciparum* parasites in malaria-positive samples, both deep learning  
398 algorithms performed with high correlation ( $r > 0.99$ ) to the manual, visual quantification of parasites  
399 in the digital samples, suggesting that the methods are comparable. Notably, a similarly high level of  
400 correlation was also observed when comparing the results from the DLSs to the qPCR-based  
401 assessment of infection level ( $r = 0.90$ ), although these results were only available for a subset of  
402 patients (S Fig 3). Overall, the number of detected signals (parasite candidates) by analysis with the



403 DLSs was low in microscopy-negative samples, and mainly corresponded to fluorescent artefacts and  
404 debris (S Fig 2). The results here suggest that it would be possible to establish an operative threshold  
405 for the DLSs to separate positive and negative samples with relatively high sensitivity. Here, using a  
406 threshold for positivity of e.g. 0.10% for detected infected RBCs, the detection of positive samples in  
407 the validation series would be possible with approximately 95% sensitivity and specificity. This could  
408 initially be useful e.g. as a triage system to automatically detect the majority of abnormal slides,  
409 although the accurate detection of low-level infections would require higher sensitivity. Our results  
410 are in line with findings from earlier studies, where fluorescence malaria field microscopy has shown  
411 promise as a field-applicable and inexpensive diagnostic technology (33). Similarly to our findings,  
412 previous work has suggested that high sensitivity (up to 98%) and reasonable sensitivity (89%) can be  
413 achieved using visual fluorescence field microscopy, compared to conventional methods, and  
414 especially for samples with high levels of parasitaemia (34). Previous work has also demonstrated  
415 how the digital analysis of DAPI-stained blood samples, digitized with a 40x objective digital  
416 microscope in laboratory conditions, can be used to quantify levels of parasitaemia and even classify  
417 the infection stage of the parasites (35). Notably, the principal challenges with equivocal fluorescent  
418 particles being detected as parasites in samples with low levels of parasitemia encountered here has  
419 also been described previously (33). Although significantly lower amounts of parasite signals were  
420 detected in the microscopy-negative samples, the levels were still relatively high compared to e.g. the  
421 detection limits of conventional Giemsa thick smear microscopy. Therefore, to achieve ideal levels of  
422 sensitivity for primary malaria diagnostics, methods to improve sensitivity for especially low-level  
423 infections are essential. These include steps to minimize sample contaminations to allow the  
424 digitization of large, representative sample areas (i.e. uncontaminated monolayers of RBCs). To  
425 achieve similar levels of sensitivity as Giemsa thick smear-microscopy and RDTs, increasing the total  
426 sample area analysed (currently ~100 high-power FOVs) or utilizing methods to increase the amounts  
427 of visible RBCs per image field are crucial.

428 As this work represents a proof-of-concept study, it has certain limitations that need to be  
429 addressed. Firstly, the principal challenge encountered here and the major cause of false-positive  
430 signals in the microscopy-negative samples was the presence of artefacts and debris in the blood

431 smears, which resulted in fluorescent signals not originating from parasites. Although the staining  
432 process described here is simple to perform, the technique is, similarly to conventional staining  
433 methods, prone to contaminations, which was challenging especially in samples with higher levels of  
434 contamination and low parasite densities (S Fig 1). This emphasizes the need for robust sample  
435 processing to ensure usability in field settings. Secondly, here, we compared the parasite  
436 quantification in stained thin blood smears to the microscopy-assessment of thick smears from the  
437 patients, and accordingly observed a certain variation in the estimated infection levels. To determine  
438 the correlation to Giemsa microscopy, the analysis of Giemsa-stained thin blood smears from the  
439 same patients would be the preferred ground truth, which was not available in the current study.  
440 Notably, when testing the algorithms on samples prepared in laboratory conditions with known levels  
441 of *P. falciparum* infection, a strong correlation ( $r > 0.99$ ,  $p < 0.001$ ) was observed in DLS-detected  
442 levels of infection and known parasitaemia (S Fig 4). Lastly, we digitized areas of the thin smears that  
443 contained representative monolayers with minimal amounts of artefacts, but in a clinical setting larger  
444 representative sample areas would be analysed to improve the sensitivity for lower-level infections.

## 445 **5 Conclusion**

446 This proof-of-concept study shows that detection and quantification of *P. falciparum* parasites  
447 in thin blood smears is feasible, using a simplified fluorescent staining process, an inexpensive, POC  
448 portable slide-scanner and a deep learning-algorithm. As digital microscopy is currently limited  
449 mainly to laboratories with access to high-end digitization equipment, this method warrants further  
450 investigation as a potential novel platform for AI-based, digital malaria microscopy at the POC. The  
451 method can facilitate microscopy diagnostics in field settings and offer the benefits that digital and  
452 automated microscopy is associated with e.g. more objective and reproducible results, potentially  
453 reduced time for needed for sample analysis (compared to the manual quantification of parasites), and  
454 a method that can be used for monitoring of treatment efficacy through assessment of parasite  
455 clearance. Also, the method is likely to be applicable for different *Plasmodium* species and other  
456 pathogens, especially those where fluorescence microscopy may offer additional diagnostic  
457 advantages.

458

459

460

461 **7 Supplementary material**

462

463 **S Figure 1.** Results from deep learning-based analysis of control samples, prepared from blood  
464 cultures in laboratory-conditions with known levels of *P. falciparum* infections (0% and  
465 approximately 0.2%, 0.5%, 1% and 2% levels of parasitemia, respectively). Correlation between  
466 results measured with the Pearson's product-moment correlation coefficient and showing an almost  
467 perfect level of correlation ( $r(7) = 0.99$ ).

468

469 **S Figure 2.** Digitized Giemsa-stained thin blood smear from patient in study cohort. Images showing  
470 sample with high amounts of visible artefacts and debris.

471

472 **S Figure 3.** Detected level of malaria infection before initiation of treatment, as determined by  
473 analysis with the deep learning-systems (DLSs), compared to quantitative PCR-based analysis of  
474 samples from a subset of patients. Correlation between results measured with the Pearson's product-  
475 moment correlation coefficient and showing a high level of correlation ( $r(27) = 0.90$ ).

476

477 **S Figure 3 (Suggestion 2).** Detected level of malaria infection before initiation of treatment, as  
478 determined by analysis with the deep learning-systems (DLSs), compared to quantitative PCR-based  
479 analysis of samples from a subset of patients. DLS-detected parasitemia calculated based on an  
480 assumed amount of 5,000,000 RBCs per  $\mu\text{L}$  of blood. Correlation between results measured with the  
481 Pearson's product-moment correlation coefficient and showing a high level of correlation ( $r(27) =$   
482  $0.90$ ).

483

484

485

486 **S Figure 4.** STARD diagram of study workflow and sample processing.

487

488 **Declaration of interests**

489 Johan Lundin and Mikael Lundin are founders and co-owners of Aiforia Technologies Oy,  
490 Helsinki, Finland. The rest of the authors declare that there are no competing interests.

491

492 **Funding statement**

493 This work was funded by the Swedish Research Council, Swedish International Development  
494 Agency (SIDA) and Sigrid Jusélius Foundation. In addition, the study has been supported by  
495 Finska Läkaresällskapet, Biomedicum Foundation, Medicinska Understödsföreningen Liv  
496 och Hälsa rf, the Nvidia Corporation and Wilhelm och Elsa Stockmanns stiftelse. We  
497 furthermore greatly acknowledge the assistance and support from the Helsinki Institute of  
498 Life Science (HiLIFE) and the FIMM Digital Microscopy and Molecular Pathology Unit  
499 supported by Helsinki University and Biocenter Finland. The funders did not play any role in  
500 the study design, data collection and analysis, decision to publish, or preparation of the  
501 manuscript.

## 502 **8 References**

- 503 (1) World Health Organization. World Malaria Report 2018. 2018 19 november.
- 504 (2) Charpentier E, Benichou E, Pagès A, Chauvin P, Fillaux J, Valentin A, et al. Performance  
505 evaluation of different strategies based on microscopy techniques, rapid diagnostic test and molecular  
506 loop-mediated isothermal amplification assay for the diagnosis of imported malaria. *Clinical  
507 Microbiology and Infection* 2020;26(1):115-121.
- 508 (3) World Health Organization. Guidelines for the treatment of malaria, 3rd ed. 2015.
- 509 (4) Mathison BA, Pritt BS. Update on Malaria Diagnostics and Test Utilization. *J Clin Microbiol*  
510 2017;55(7):2009-2017.
- 511 (5) World Health Organization. Malaria microscopy quality assurance manual – Ver. 2. 2016 January.
- 512 (6) Frean J, Perovic O, Fensham V, McCarthy K, von Gottberg A, de Gouveia L, et al. External  
513 quality assessment of national public health laboratories in Africa, 2002-2009. *Bull World Health  
514 Organ* 2012 Mar 01;90(3):191-199A.
- 515 (7) O'Meara WP, Barcus M, Wongsrichanalai C, Muth S, Maguire JD, Jordan RG, et al. Reader  
516 technique as a source of variability in determining malaria parasite density by microscopy. *Malaria  
517 Journal* 2006 Dec 12;5:118.
- 518 (8) Wongsrichanalai C, Barcus MJ, Muth S, Sutamihardja A, Wernsdorfer WH. A review of malaria  
519 diagnostic tools: microscopy and rapid diagnostic test (RDT). *American Journal of Tropical Medicine  
520 & Hygiene* 2007 Dec;77(6 Suppl):119-127.
- 521 (9) Leski TA, Taitt CR, Swaray AG, Bangura U, Reynolds ND, Holtz A, et al. Use of real-time  
522 multiplex PCR, malaria rapid diagnostic test and microscopy to investigate the prevalence of  
523 *Plasmodium* species among febrile hospital patients in Sierra Leone. *Malaria Journal* 2020;19(1):84.
- 524 (10) Mhamilawa LE, Aydin-Schmidt B, Mmbando BP, Ngasala B, Morris U. Detection of  
525 *Plasmodium falciparum* by Light Microscopy, Loop-Mediated Isothermal Amplification, and  
526 Polymerase Chain Reaction on Day 3 after Initiation of Artemether–Lumefantrine Treatment for  
527 Uncomplicated Malaria in Bagamoyo District, Tanzania: A Comparative Trial. *The American Journal  
528 of Tropical Medicine and Hygiene*, 2019;101(5):1144-1147.

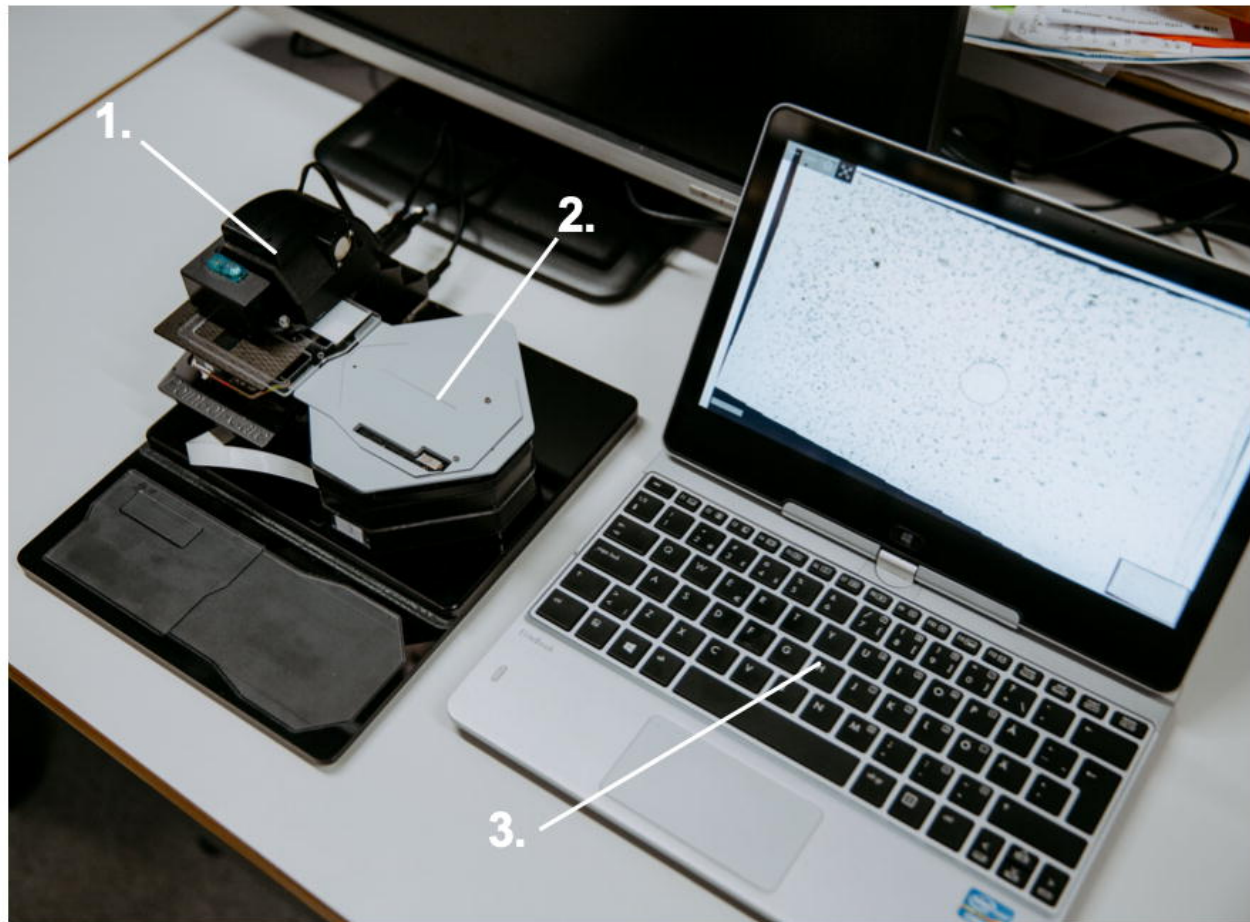
- 529 (11) Guy R, Liu P, Pennefather P, Crandall I. The use of fluorescence enhancement to improve the  
530 microscopic diagnosis of falciparum malaria. *Malaria Journal* 2007;6(1):89.
- 531 (12) Wongsrichanalai C, Kawamoto F. Fluorescent Microscopy and Fluorescent Labelling for Malaria  
532 Diagnosis. In: Hommel M, Kremsner PG, editors. *Encyclopedia of Malaria* New York, NY: Springer  
533 New York; 2021. p. 1-7.
- 534 (13) Boppart SA, Richards-Kortum R. Point-of-care and point-of-procedure optical imaging  
535 technologies for primary care and global health. *Science Translational Medicine* 2014;6(253):253rv2.
- 536 (14) International Telecommunication Union. *ICT Facts and Figures - The World in 2015*. 2015;  
537 Available at: <https://www.itu.int/en/ITU-D/Statistics/Documents/facts/ICTFactsFigures2015.pdf>.  
538 Accessed 20.11., 2019.
- 539 (15) J. C. Contreras-Naranjo, Q. Wei, A. Ozcan. Mobile Phone-Based Microscopy, Sensing, and  
540 Diagnostics. *IEEE Journal of Selected Topics in Quantum Electronics* 2016;22(3):1-14.
- 541 (16) Digital Pathology Association, 2020. Digital Pathology FAQ. Electronic resource, available on:  
542 <https://digitalpathologyassociation.org/faq> [Retrieved on June 21th, 2020].
- 543 (17) Holmstrom O, Linder N, Ngasala B, Martensson A, Linder E, Lundin M, et al. Point-of-care  
544 mobile digital microscopy and deep learning for the detection of soil-transmitted helminths and  
545 *Schistosoma haematobium*. *Glob Health Action* 2017 Jun;10(sup3):1337325.
- 546 (18) Holmstrom O, Linder N, Moilanen H, Suutala A, Nordling S, Stahls A, et al. Detection of breast  
547 cancer lymph node metastases in frozen sections with a point-of-care low-cost microscope scanner.  
548 *PLoS ONE* [Electronic Resource] 2019;14(3):e0208366.
- 549 (19) Bera K, Schalper KA, Rimm DL, Velcheti V, Madabhushi A. Artificial intelligence in digital  
550 pathology — new tools for diagnosis and precision oncology. *Nature Reviews Clinical Oncology*  
551 2019;16(11):703-715.
- 552 (20) Moon S, Lee S, Kim H, Freitas-Junior L, Kang M, Ayong L, et al. An image analysis algorithm  
553 for malaria parasite stage classification and viability quantification. *PloS one* 2013;8(4):e61812.
- 554 (21) Linder N, Turkki R, Walliander M, Martensson A, Diwan V, Rahtu E, et al. A malaria diagnostic  
555 tool based on computer vision screening and visualization of *Plasmodium falciparum* candidate areas  
556 in digitized blood smears. *PLoS ONE* [Electronic Resource] 2014;9(8):e104855.

- 557 (22) Poostchi M, Silamut K, Maude RJ, Jaeger S, Thoma G. Image analysis and machine learning for  
558 detecting malaria. *Translational Research: The Journal Of Laboratory & Clinical Medicine*  
559 2018;194:36-55.
- 560 (23) Mhamilawa LE, Ngasala B, Morris U, Kitabi EN, Barnes R, Soe AP, et al. Parasite clearance,  
561 cure rate, post-treatment prophylaxis and safety of standard 3-day versus an extended 6-day treatment  
562 of artemether-lumefantrine and a single low-dose primaquine for uncomplicated *Plasmodium*  
563 *falciparum* malaria in Bagamoyo district, Tanzania: a randomized controlled trial. *Malaria journal*  
564 2020;19(1):216.
- 565
- 566 (24) World Health Organization. Malaria Parasite Counting. Malaria Microscopy Standard Operating  
567 Procedure. 2016; Available at:  
568 [http://www.wpro.who.int/mvp/lab\\_quality/2096\\_oms\\_gmp\\_sop\\_09\\_rev1.pdf](http://www.wpro.who.int/mvp/lab_quality/2096_oms_gmp_sop_09_rev1.pdf). Accessed 20.11., 2019.
- 569 (25) Konsti J, Lundin M, Linder N, Haglund C, Blomqvist C, Nevanlinna H, et al. Effect of image  
570 compression and scaling on automated scoring of immunohistochemical stainings and segmentation  
571 of tumor epithelium. *Diagnostic Pathology* 2012;7:29.
- 572 (26) A. Natan, Fast 2D peak finder, MATLAB Central File Exchange, 2013. Available at:  
573 <https://www.mathworks.com/matlabcentral/fileexchange/37388-fast-2d-peak-finder>
- 574 (27) Z. Wang, A. C. Bovik, H. R. Sheikh, and E. P. Simoncelli, "Image Quality Assessment: From  
575 Error Visibility to Structural Similarity," *IEEE Transactions on Image Processing*, Volume 13, Issue  
576 4, pp. 600- 612, 2004.
- 577 (28) Tajbakhsh N, Shin J, Gurudu S, Hurst RT, Kendall C, Gotway M, et al. Convolutional Neural  
578 Networks for Medical Image Analysis: Fine Tuning or Full Training? *IEEE Trans Med Imaging*  
579 2016;35:1.
- 580 (29) Szegedy C, Liu W, Jia Y, Sermanet P, Reed S, Anguelov D, et al. Going deeper with  
581 convolutions. ; 2015.
- 582 (30) Faul F, Erdfelder E, Lang A, Buchner A. G\*Power 3: A flexible statistical power analysis  
583 program for the social, behavioral, and biomedical sciences. *Behavior Research Methods* 2007(39  
584 (2)):175-191.

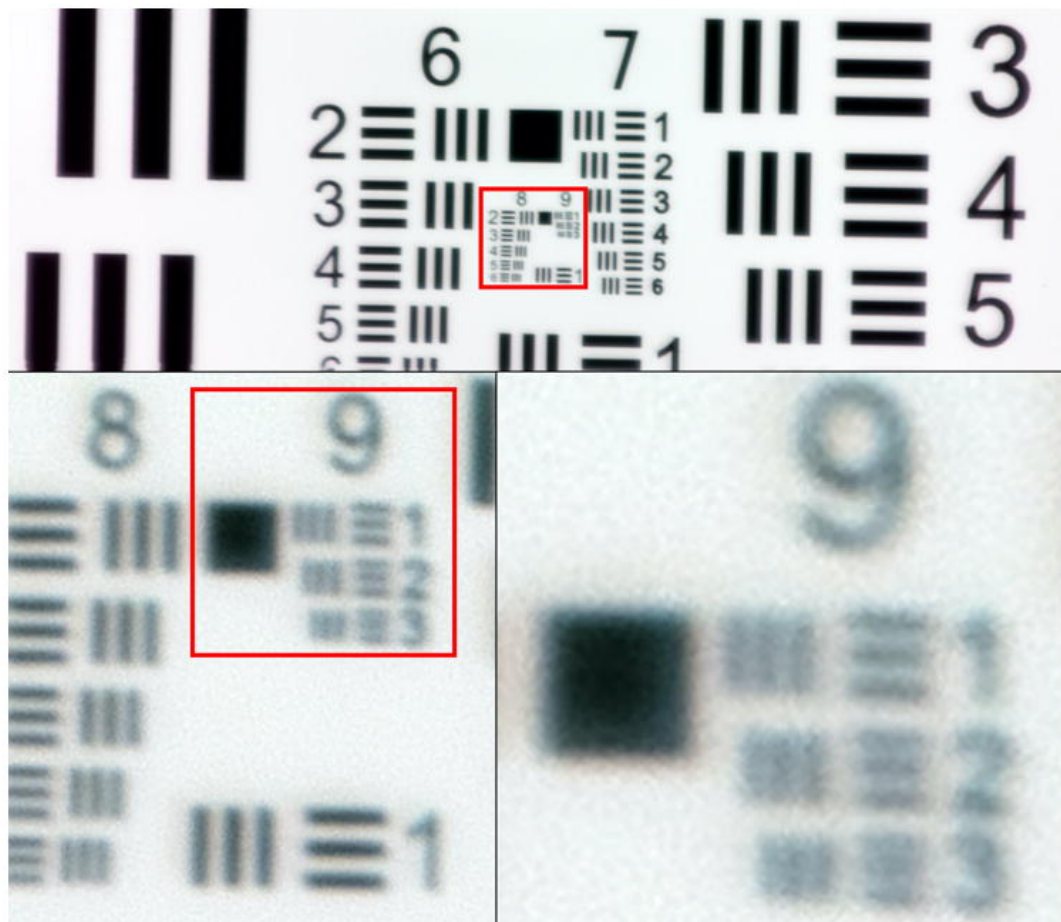


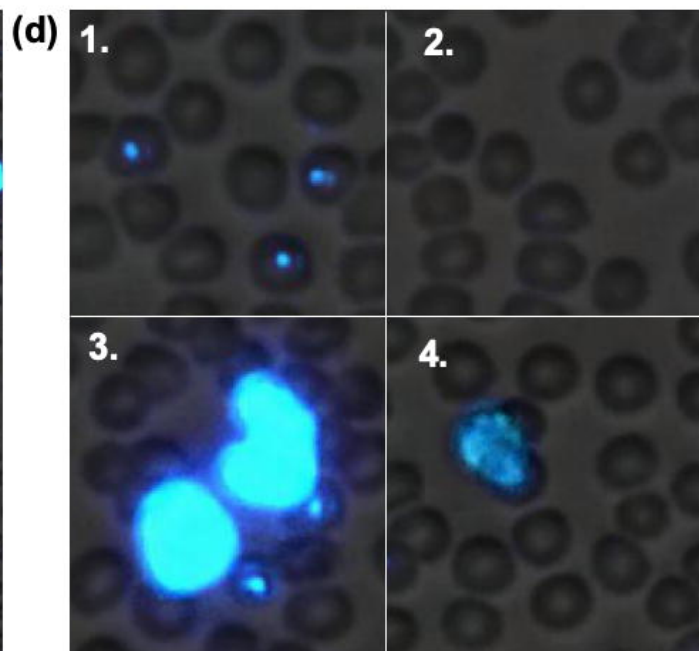
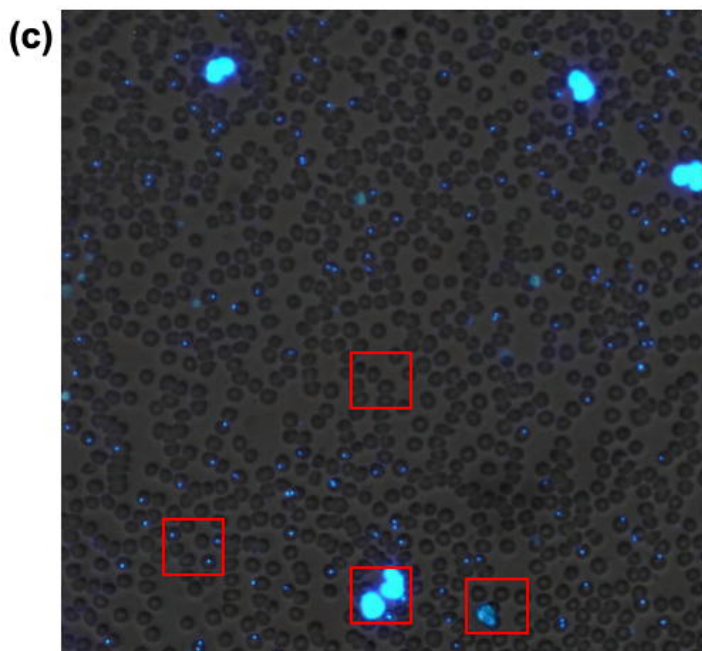
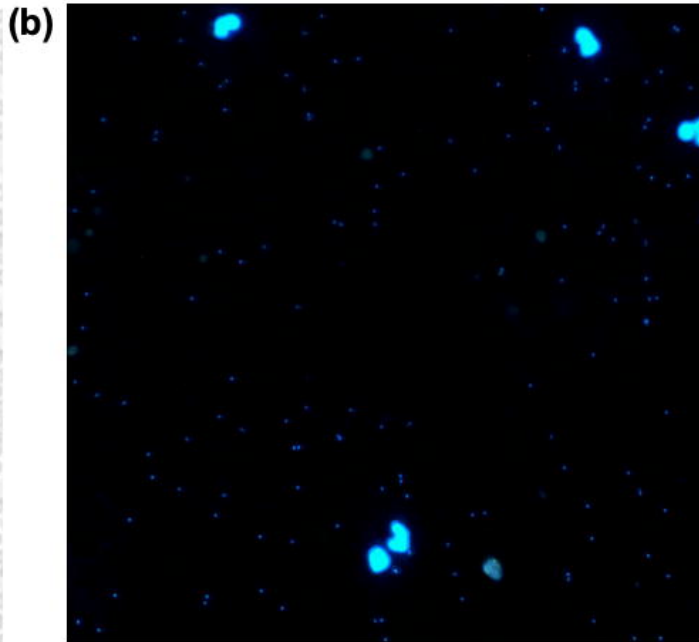
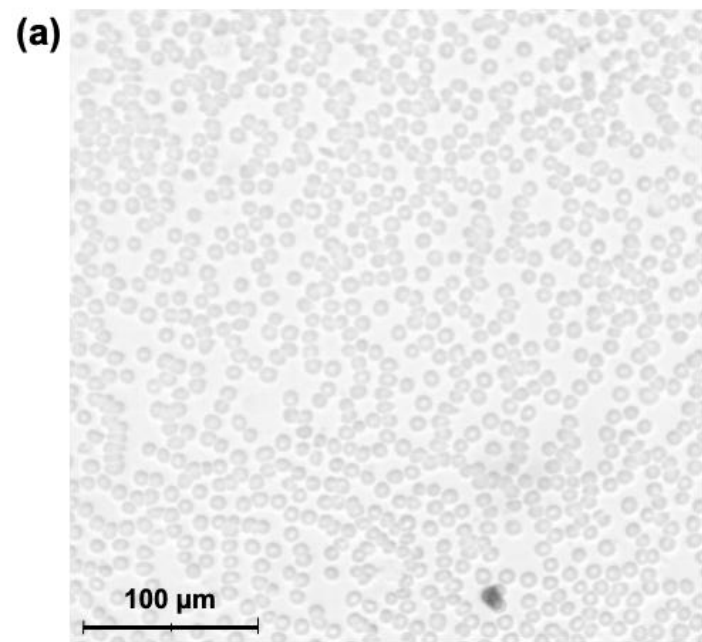
- 585 (31) Bejon P, Andrews L, Hunt-Cooke A, Sanderson F, Gilbert SC, Hill AVS. Thick blood film  
586 examination for Plasmodium falciparum malaria has reduced sensitivity and underestimates parasite  
587 density. Malaria journal 2006;5:104.
- 588 (32) O'Meara W, McKenzie F, Magill A, Forney J, Permpanich B, Lucas C, et al. Sources of  
589 variability in determining malaria parasite density by microscopy. Am J Trop Med Hyg 2005;73:593-  
590 8.
- 591 (33) Sousa-Figueiredo, J.C., Oguttu, D., Adriko, M., Besigye, F., Nankasi, A., Arinaitwe, M.,  
592 Namukuta, A., Betson, M., Kabatereine, N.B. & Stothard, J.R. 2010, "Investigating portable  
593 fluorescent microscopy (CyScope) as an alternative rapid diagnostic test for malaria in children and  
594 women of child-bearing age", Malaria journal, vol. 9, pp. 245-245.
- 595 (34) Hassan, S., Haggaz, A., Mohammed-Elhassan, E., Malik, E. & Adam, I. 2011, "Fluorescence  
596 microscope (Cyscope®) for malaria diagnosis in pregnant women in Medani Hospital, Sudan",  
597 Diagnostic pathology, vol. 6, pp. 88.
- 598 (35) Moon S, Lee S, Kim H, Freitas-Junior L, Kang M, Ayong L, et al. An image analysis algorithm  
599 for malaria parasite stage classification and viability quantification. PloS one 2013;8(4):e61812.

(a)

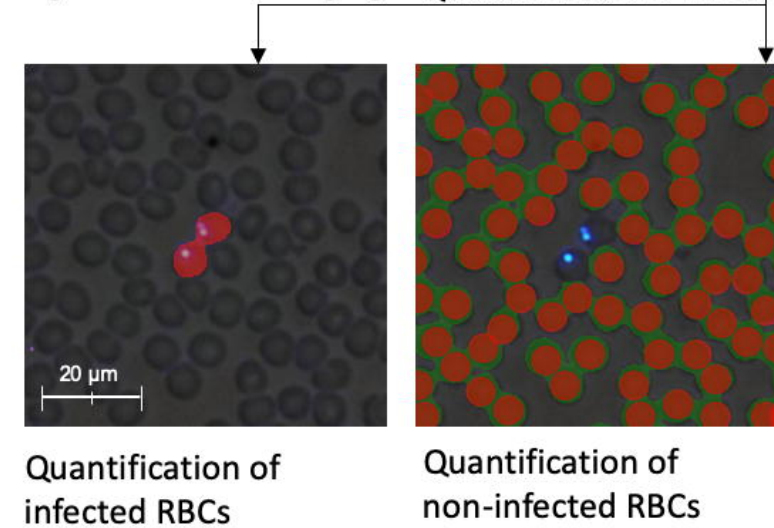
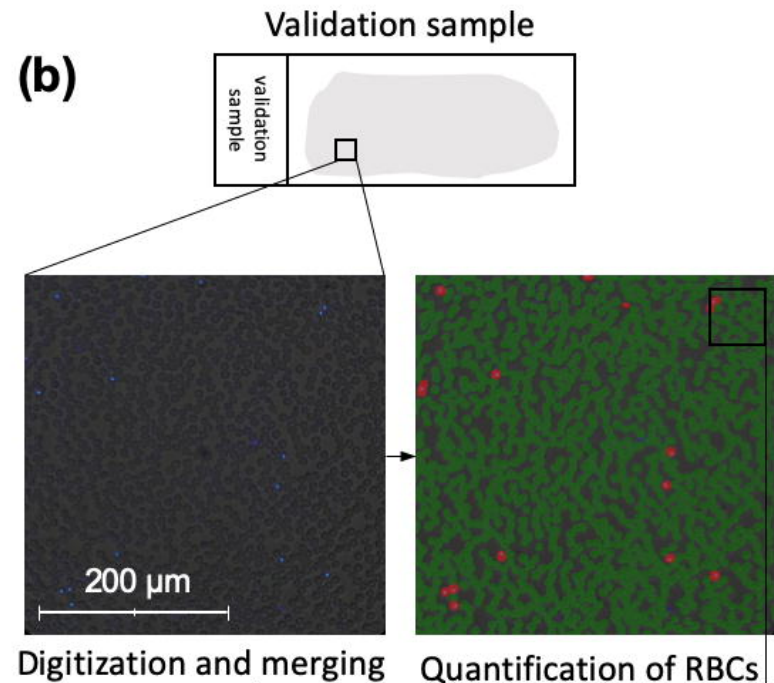
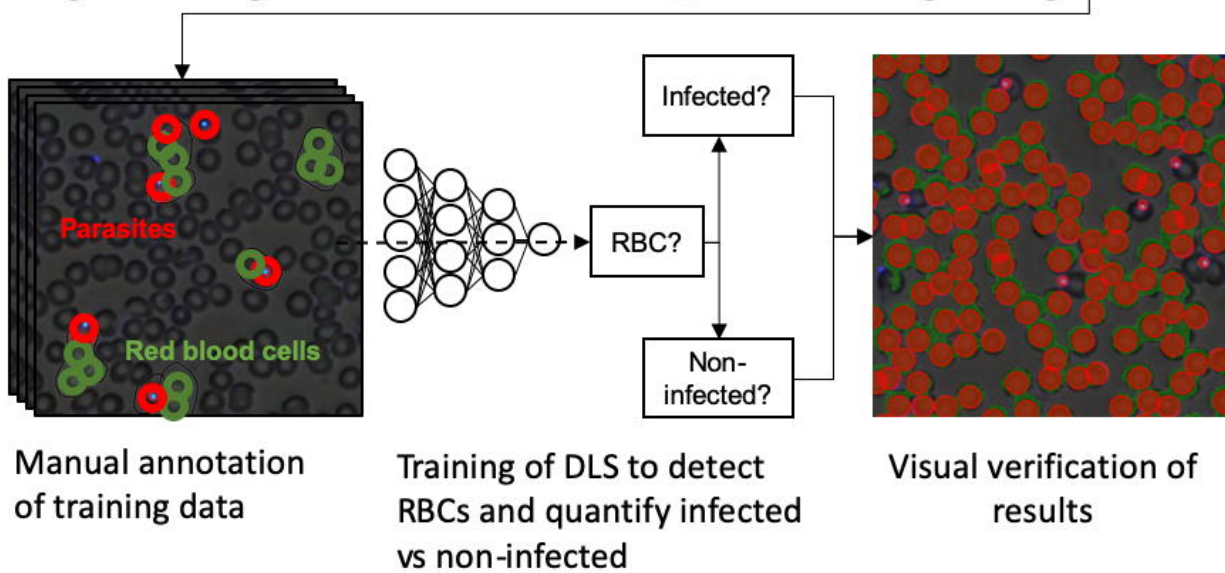
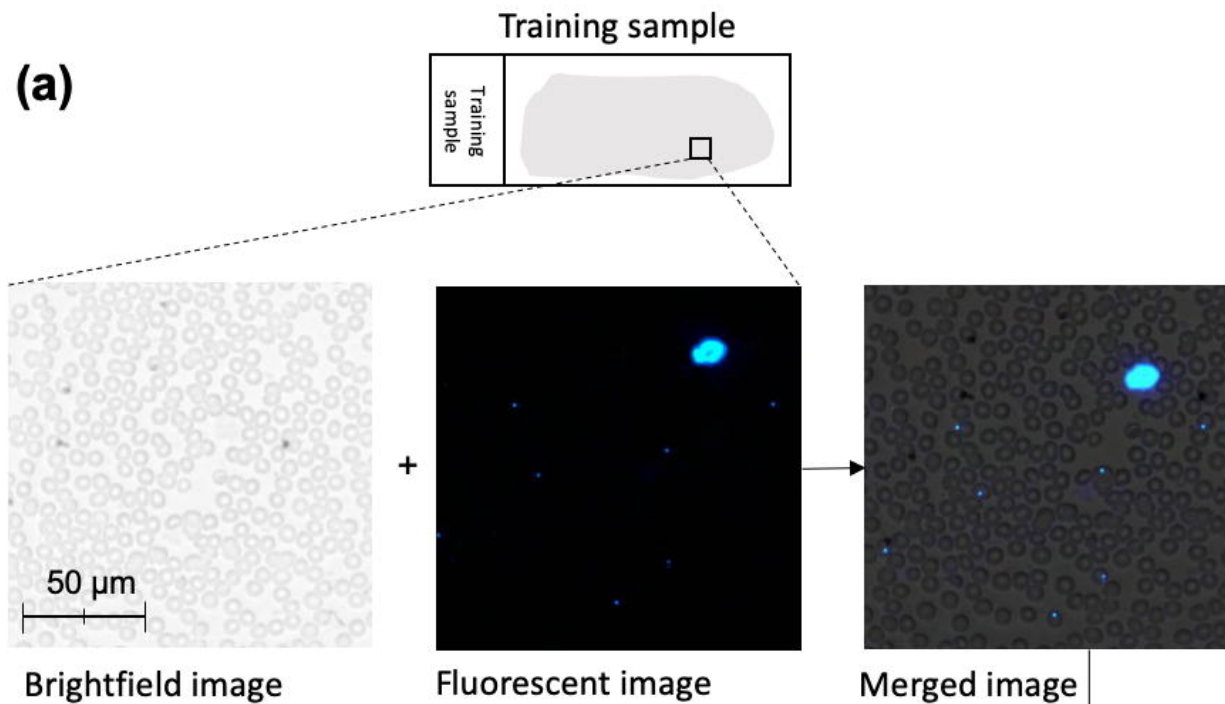


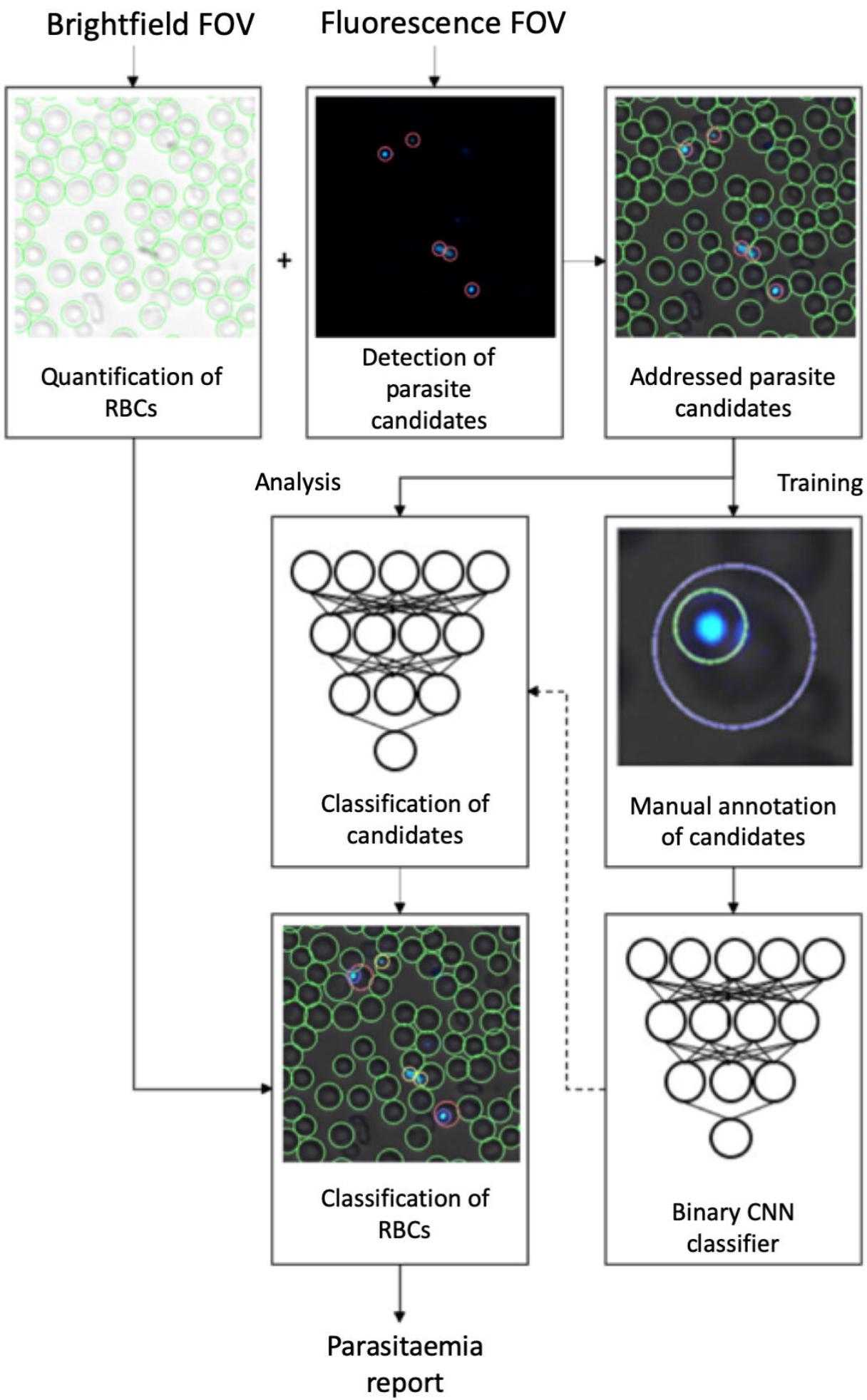
(b)



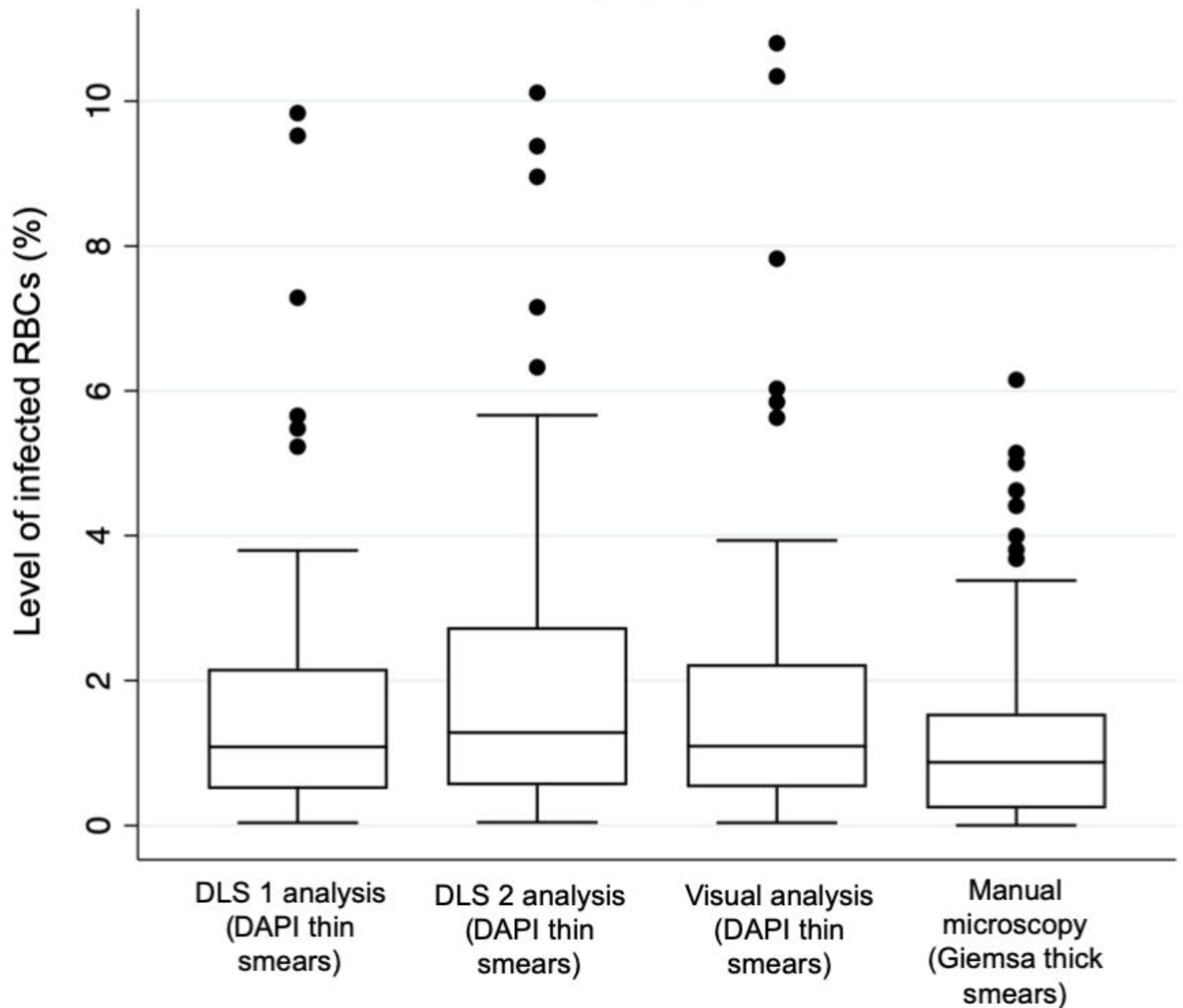






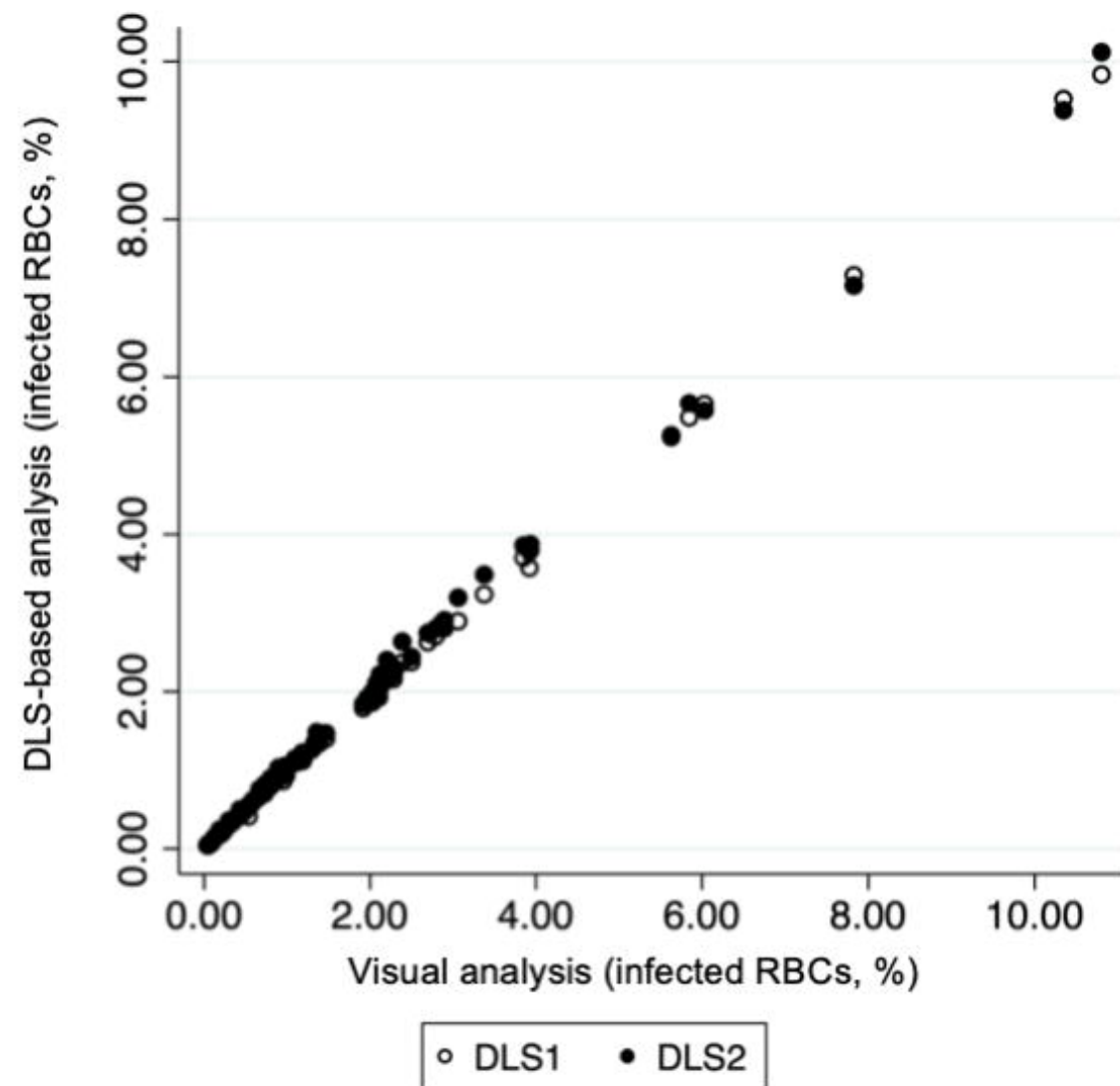


Detected *P. falciparum* parasitemia  
(Day 0)

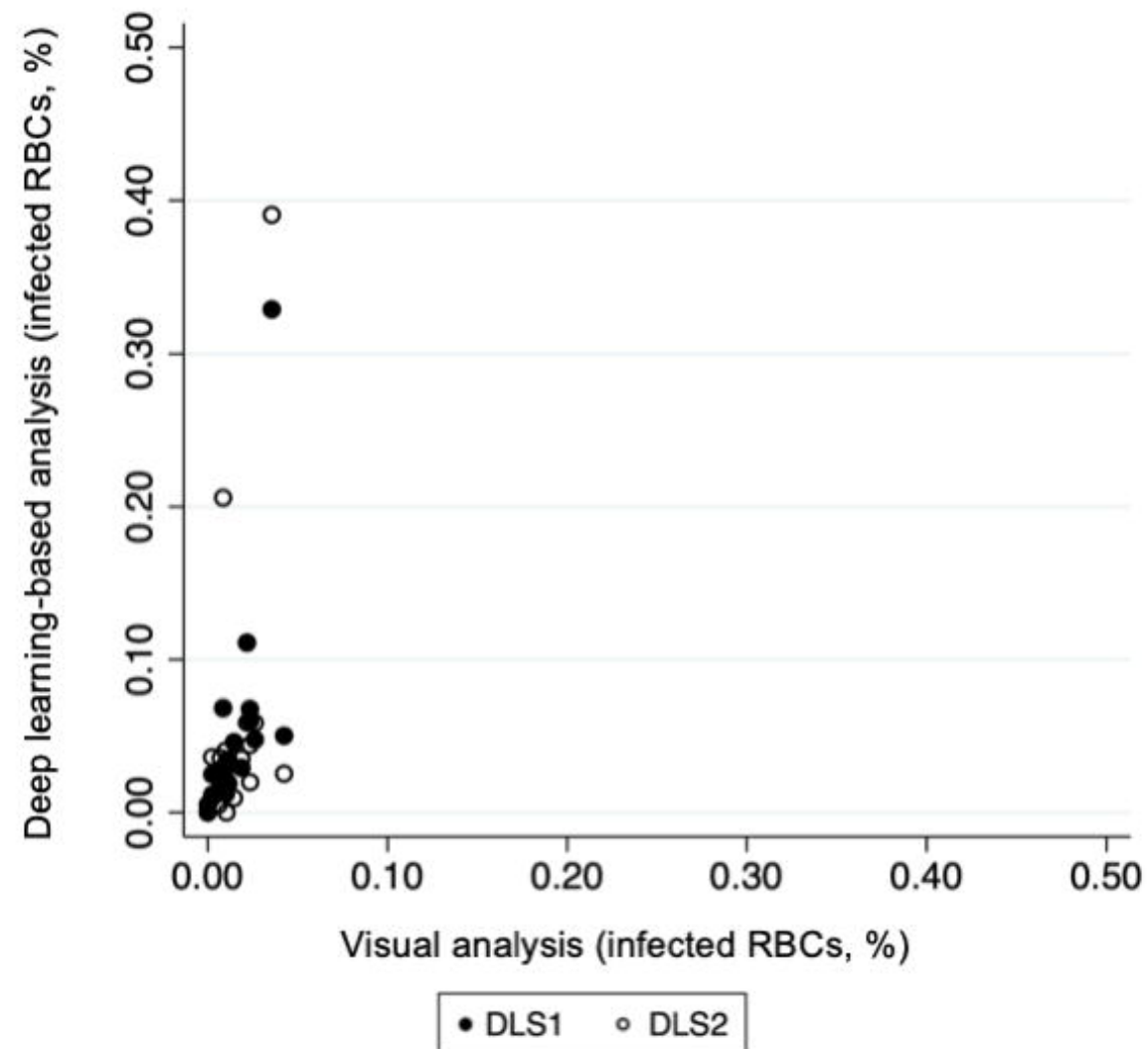


**a.**

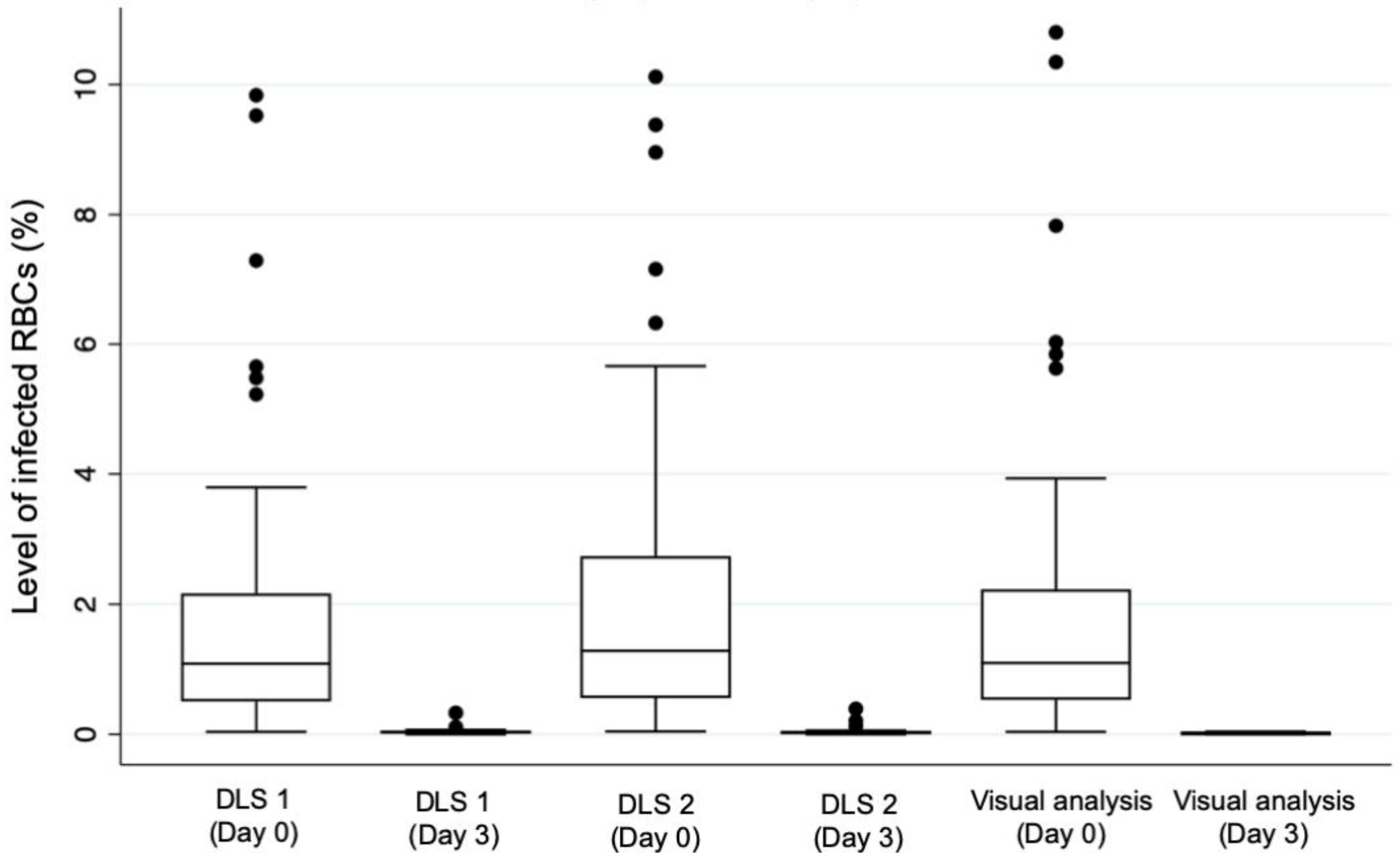
Detected *P. falciparum* parasitemia  
(Day 0)

**b.**

Detected *P. falciparum* parasitemia  
(Day 3)

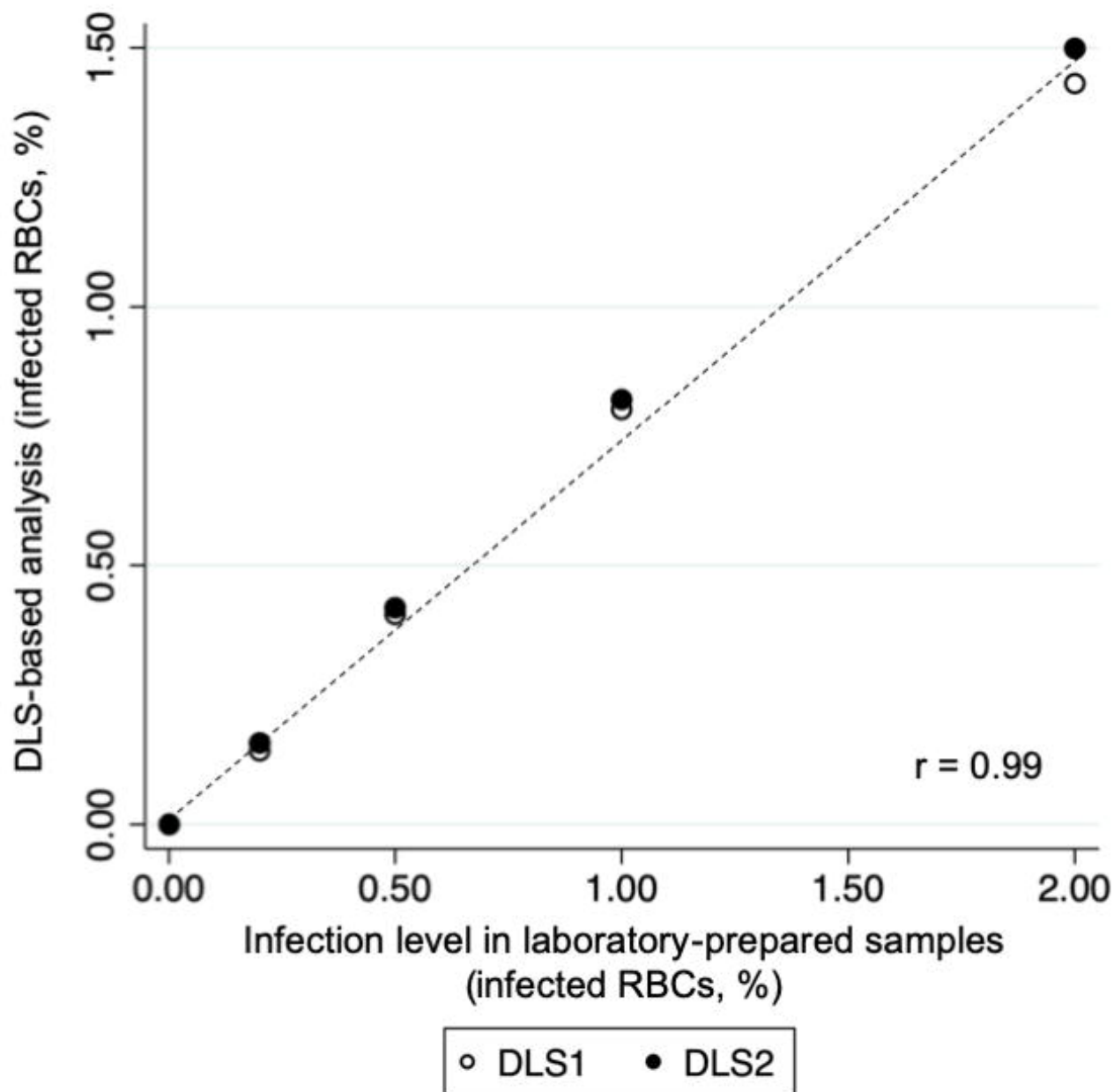


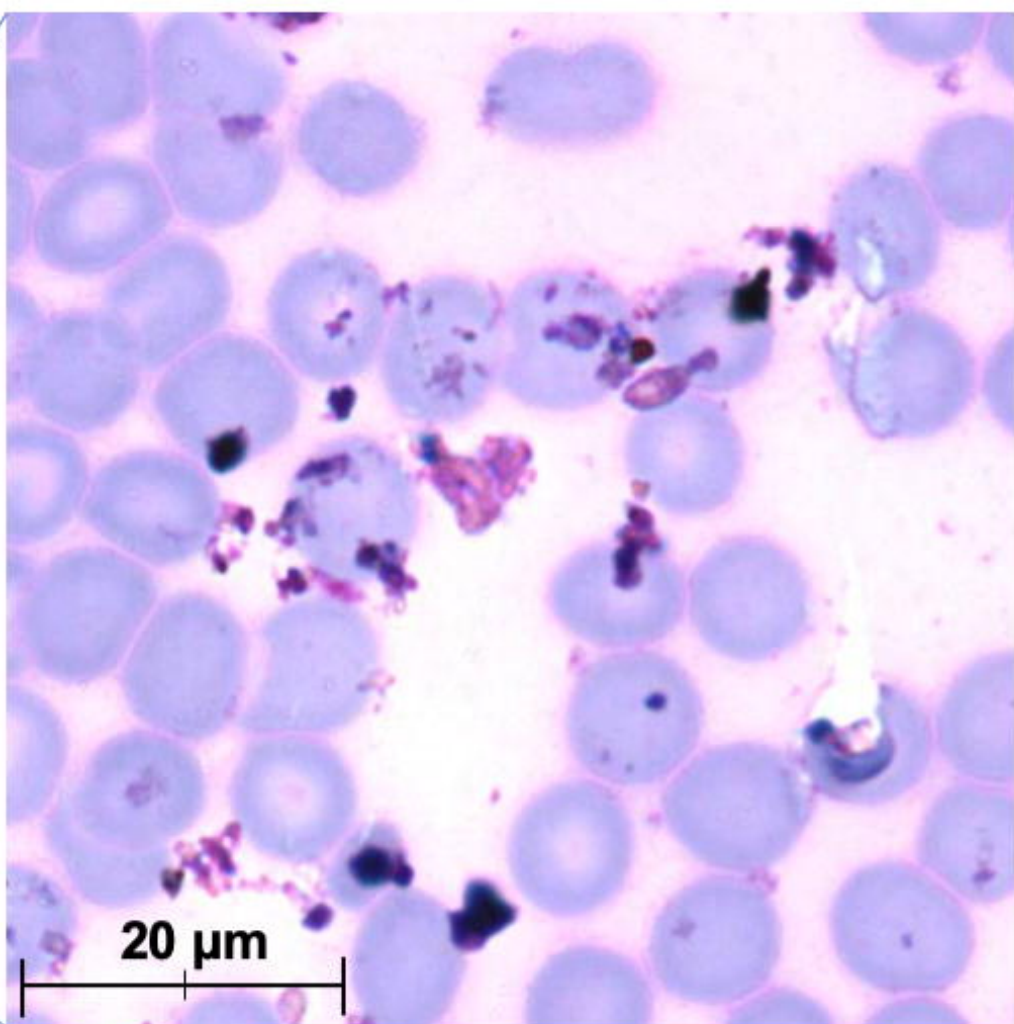
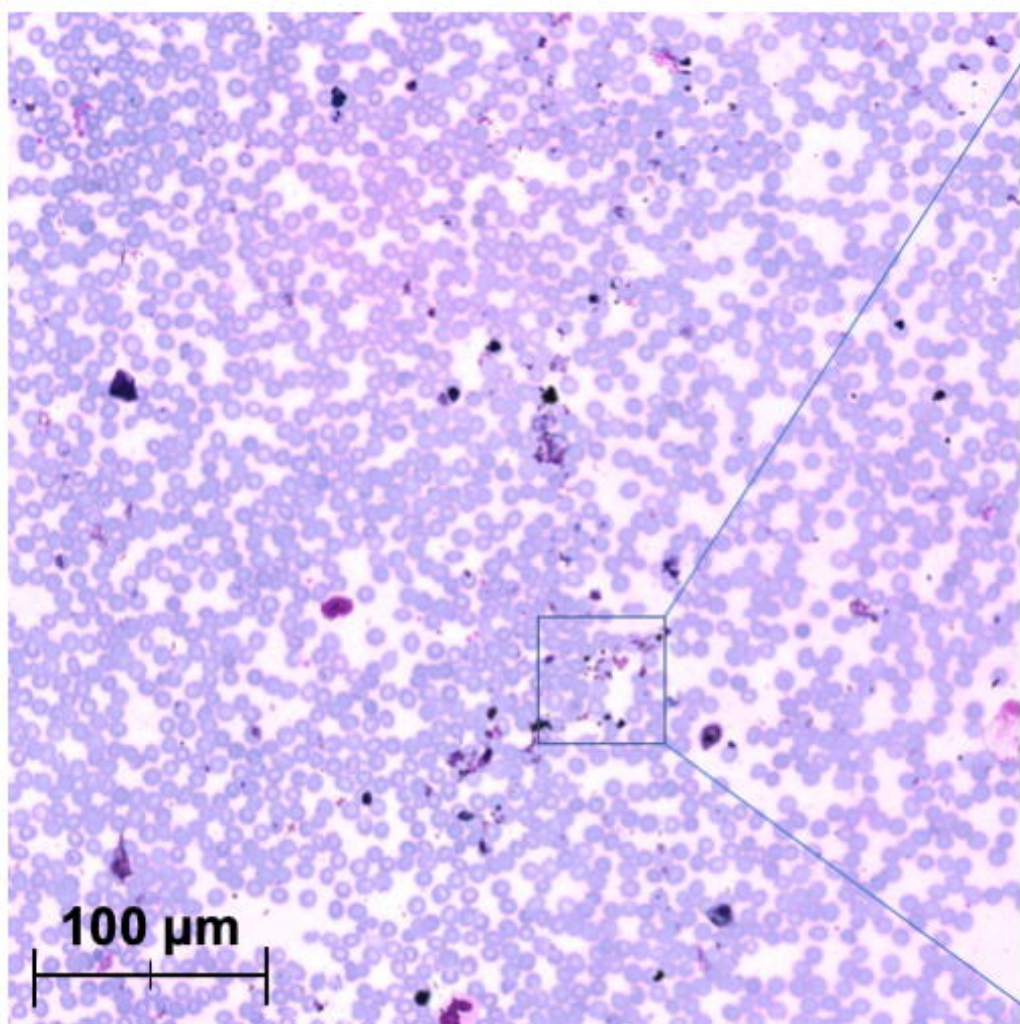
Detected *P. falciparum* parasitemia  
(Day 0 and Day 3)



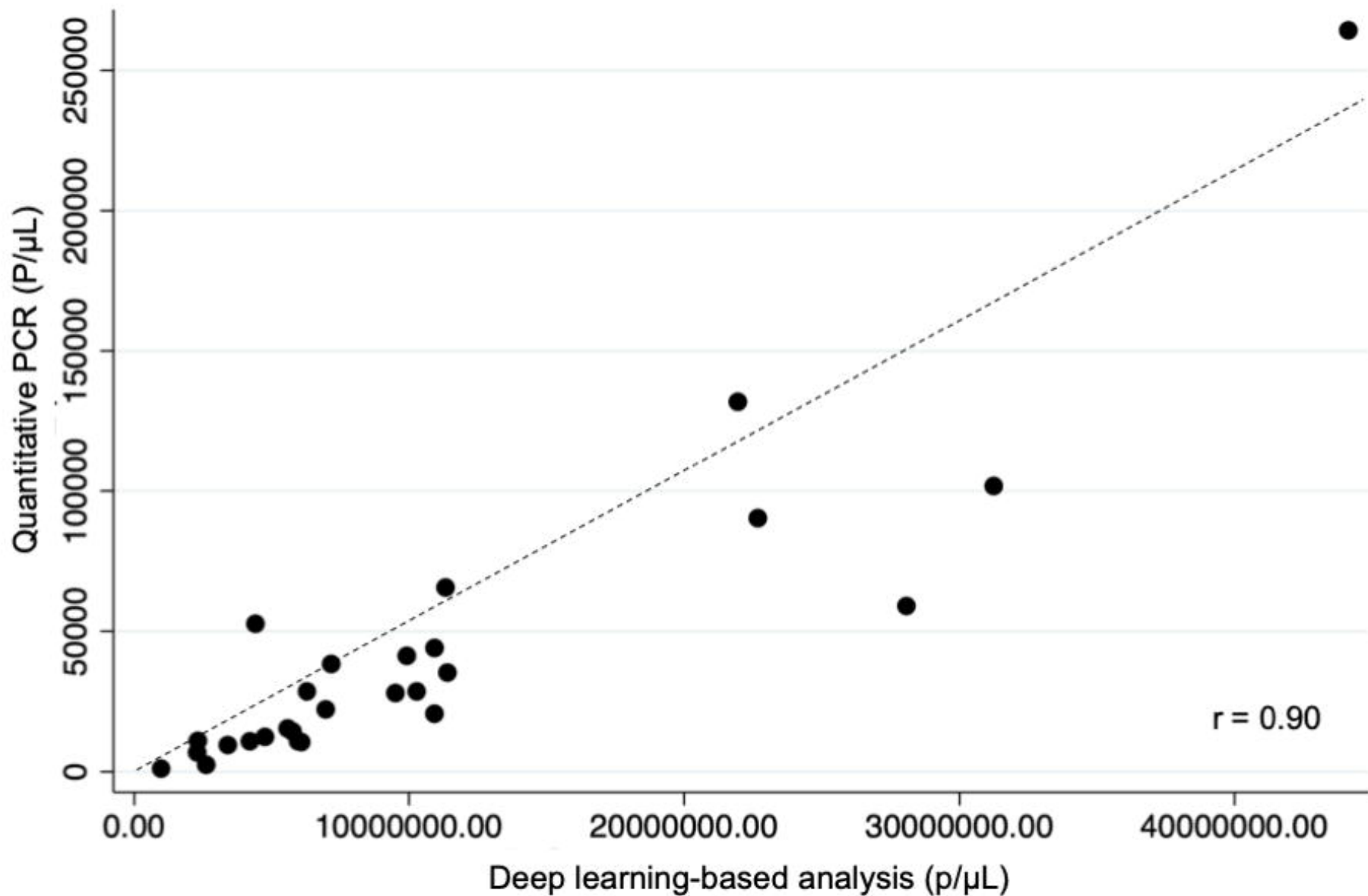


Detected *P. falciparum* parasitemia  
(Control samples)





# Detected *P. falciparum* parasitemia



## STARD diagram of study workflow

